Investigating the Internal Magnetic Field of $CoTa_2O_6$

Using Muon Spin Relaxation

Ethan D Robinson

A senior thesis submitted to the faculty of
Brigham Young University
in partial fulfillment of the requirements for the degree of

Bachelor of Science

Benjamin Frandsen, Advisor

Department of Physics and Astronomy

Brigham Young University

ABSTRACT

Investigating the Internal Magnetic Field of $CoTa_2O_6$
Using Muon Spin Relaxation

Ethan D Robinson
Department of Physics and Astronomy, BYU
Bachelor of Science

By using Muon Spin Relaxation, we have been able to probe the internal magnetic structure of $CoTa_2O_6$, in the hope of obtaining a greater understanding of these properties and, in particular, obtaining a better understanding of magnetic transition in low dimensional materials like this. Our research was collected using data gathered from the TRIUMF fast continuous Muon source in British Columbia. When a muon interacts with the atomic structure of a sample, it decays into an electron, emitted along the vector of the muon's spin. By detecting these electrons (or, more correctly, positrons, as we use positive-muons in our expirements), at various angles and times around the perimeter, we can describe the magnetic field inside the sample. By varying the temperature of our sample, we determined where Anti-ferromagnetic behavior begins, and the behavior of the transition. Taking the raw data coming in from Canada, We best fit a curve to the detection rates. We observed the changing rate of reflection as we lowered the temperature, and discovered that the cutoff temperature for anti-ferromagnetic behavior was between 5K to 7K. Using this research, we hope that we will be able to better understand the properties of these unusual materials.

Keywords: Muon Spin Relaxation, Low Dimensionality, Antiferromagnetism, Paramagnetisim, Neel Temperature, Muon Spectroscopy

ACKNOWLEDGMENTS

To Dr. Ben Frandsen, who took me in when nobody else wanted to. To my Parents who stood by me when everything looked so dark. The $CoTa_2O_6$ was synthesized in powdered form by Dr. Hari Nair of the University of Texas, El Paso. All Experiments were performed by members of the Frandsen Research Group at the TRIUMF lab in Vancouver, British Columbia. Additional Acknowledgments go to my Parents, who have stood by me through this long and difficult process

Contents

Chapter 1

Introduction

1.1 Overview

The purpose of this thesis is to analyze the internal magnetic structure of $CoTa_2O_6$ using Muon Spin Relaxation. Before we describe the technical details of this experiment and its results, it would be beneficial to briefly review some of the scientific principles that we will employ. Namely, we discuss the physical basis of the internal magnetic field, including the muon particle that we used as our magnetic probe in this experiment, and the specific crystal structure of $CoTa_2O_6$. All of these principles will have a great impact on our research and are vital for understanding our results.

1.1.1 Physical Basis

The orbits of electrons around the entrenched nuclei in a crystalline structure can clump together to create groupings known as magnetic domains. As one would expect, the random nature of the domains (a result of quantum indeterminacy) can cause a great deal of fluctuations in the internal magnetic field inside the material. It is the sum-total effects of these domains that give magnetic materials their macroscopic quantities, from the powerful magnets used in experimental fusion

reactors to the ones stuck to your refrigerator [1]. By seeking a greater understanding of the formation and evolution of domains (sometimes known as magnetic order), we hope to provide a path to better and more efficient magnetic materials. Potential applications of this research will be discussed at the end of this thesis

As one would expect, the magnetic moments of these domains, external magnetic fields, and the magnetic effect of charged particles are all intertwined, resulting in a dramatic effect upon the magnetic properties of charged particles trapped inside the crystalline structure. We used this effect to our advantage: by examining the magnetic evolution of charged particles over time, including changes in the spin vector, we can determine the strength and disposition of the local magnetic field. Then, examining the statistical makeup of these changes, we were able to determine what principles were affecting the magnetic structure of a sample crystal and how that structure changed in response to outside conditions, such as temperature or an external field.

1.1.2 The Internal Magnetic Field

The internal magnetic field of a crystal can behave in several different ways. Here is a brief overview of these behaviors.

Paramagnetism is the behavior in which the individual domains align their magnetic moments to an applied magnetic field. Since it is dependent upon unpaired (or a least, high energy) electrons, it is most prominent at high temperatures relative to absolute zero, including our subject, $CoTa_2O_6$ [2], which displays Paramagnetic behavior above apx. 70 K.

Diamagnetism is the behavior in which the individual domains of our crystal *counter-align* their magnetic moments to an applied magnetic field [2].

Ferromagnetic substances, within a certain temperature range, can maintain a net internal magnetic field, even if the outside applied field is zero [1], and is usually displayed below a certain temperature (known as the *Curie Point*). This is due to the overall magnetic moment of the component domains being a non-zero-sum, particularly if an external magnetic field had been applied to the crystal beforehand [2]. Permanent magnets are an example of fully aligned ferromagnetism.

Antiferromagnetism occurs when the domains of a crystal align in an alternating pattern. This occurs below the materials *Neel Temperature* (T_N) and creates an ordered array of domains with no overall magnetic moment in the absence of an applied field.

1.1.3 Hyperfine Field

An applied Magnetic field can induce a subsequent Hyperfine Field inside the material [3]. This Hyperfine field is a result of spin-spin interactions between the various charged particles, particularly the electrons and protons that make up the crystal atoms, and is almost always several orders of magnitude weaker than the other contributing factors in the internal magnetic field [4].

1.2 Some Important Points About the Nature of the Muon

1.2.1 The Muon Particle

The muon (μ) is a lepton approximately 207 times heavier than the electron and with the same charge and spin [4] and with an approximate lifetime of 2.18 μs [3]. The positive-muon (μ^+) is the anti-particle associated with the normal matter muon and has an equivalent charge with the positron

(e^+) [5].

The muon was first been detected by Theodor Wulf, a Jesuit Priest teaching in Valkenburg [7], who noted that an Electrometer (an instrument that measures the ionization produced by radioactivity) discharged more frequently at the top of the Eiffel Tower than at the bottom [8][1]. This phenomenon soon became known as *cosmic rays* [3]. In 1936 two researchers at the California Institute of Technology, Carl Anderson and Seth Neddermeyer, correctly identified the muon (then called the mesotron) as a core component of these cosmic rays and correctly measured its mass as one-ninth of a proton [9]. The initial identification of the muon with the mass of the proton proved to be prescient since it is usually better to think of the positive muon as a very light proton, rather than as a member of the electron family [3].

To wit, when a negative muon is inserted into a normal matter, it is attracted to the atomic nuclei that form the medium's crystalline structure. Since the mass of a muon is so much greater than

[1]This finding was later confirmed by attaching electrometers to weather balloons before raising them into the upper atmosphere

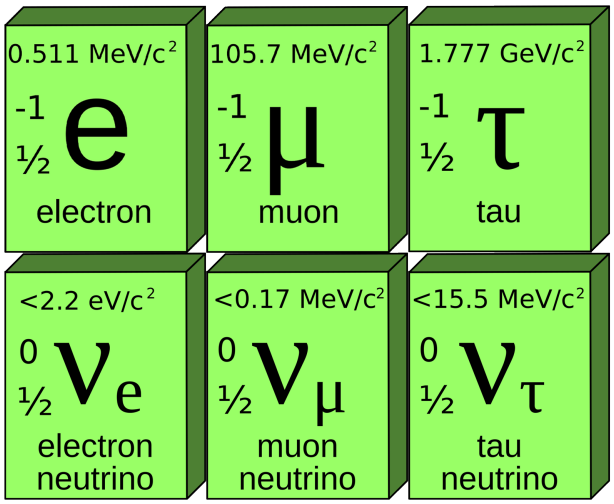

Figure 1.1 Leptons of the Standard Model [6]

the mass of an electron, it quickly drops down to the lowest (1s) energy state, where it then either decays into an electron or is captured by a proton...

$$\mu^- + p \rightarrow n + \nu_\mu \tag{1.1}$$

Conversely, when the positive muon is inserted into a crystalline structure, the Coulomb interaction repels it away from the various nuclei. The muon first sheds most of its energy (on the order of several KeV) ionizing the nearby atoms on its path through the material. After coming to rest at an interstitial site, the muon then undergoes a series of electron capture and release reactions, reducing its energy to just a few electron volts. This entire reaction chain takes place in a few hundred picoseconds [3]. As a result, of this behavior, positive muons are used when detecting internal magnetic fields using Muon Spin Relaxation (μSR). We will discuss this particular technique further in section 2.

1.2.2 Larmor Precession

Like the proton, the positive neutron is a positively charged particle. The spin of a charged particle creates a magnetic dipole **m** proportional to its spin angular momentum **S** [4]...

$$\mathbf{m} = \gamma \cdot \mathbf{S} \tag{1.2}$$

where γ is the gyromagnetic behavior of the particle. The exact reasons behind this proportional constant are beyond the scope of this thesis. It's enough to know that the gyromagnetic ratio of a muon is 84.8 kHz G^{-1} [3]. When this magnetic dipole interacts with a magnetic field **B**, it experiences a torque, which tries to line the particle's spin up with the external magnetic field. Classically, a torque on a spinning object will cause it to process around the vector of the applied forces: This is why the axis of a top rotates around the normal axis of the surface it's spinning on.

In this case, the effect is purely quantum[2], with an angular frequency given by [4]...

$$\omega = \gamma B \tag{1.3}$$

Thus, by knowing the frequency of the particle's precession, we were able to find the strength of the applied magnetic field.

1.3 The Crystal Structure of $CoTa_2O_6$ and My Contributions

1.3.1 Low Dimensionality

As a crystalline material, Cobalt Tantalum Oxide has a highly anisotropic molecular structure (lacking in rotational symmetry). This is an exotic system and has Ising or Heisenberg interactions along chains of magnetic moments. As a result, the magnetic moments of the various domains are aligned most strongly along a single axis [10].

We can see this reflected in the crystalline structure of our sample. $CoTa_2O_6$ is *trirulite*[3], and thus its chemical structure is rutile in nature, with six attached oxygen anions. As a result, its structure is tetragonal (identical in two axes), with the third axis three times the length of the other two.

In $CoTa_2O_6$ this causes the Co^{2+} cations to form chains along the longer axis. At low temperatures, where $CoTa_2O_6$ behaves in an anti-ferromagnetic manner, these chains will be the dominant force in the internal magnetic field, which will be highly mono-directional, albeit with alternating anti-parallel domains [10].

For visualization, think of a steam locomotive, with tubes mostly aligned vertically up and down the body of the boiler. Like the water in those tubes, the magnetic field is constrained by the

[2]This is a result of Ehrenfest's Theorem, which states that expectation values obey classical laws [4]

[3]Materials of the general form (M)Ta_2O_6, where (M) is a transition metal.

crystalline structure to only "flow" in one direction. As a result, the combination of the internal field and an external field will differ depending upon their orientation.

1.3.2 Using Muon Spin Resonance

While the internal magnetic field of $CoTa_2O_6$ has been measured using a variety of methods, including powder x-ray diffraction (PXRD) [10] [11] and powder neutron diffraction [12], we are attempting to further illuminate their findings using Muon Spin Resonance (μSR). In particular, μSR provides for a more holistic view into the internal behavior of samples; for instance, samples that may not be fully in one magnetic behavior or the other, or samples whose constituent parts not be fully aligned. Again, a more complete description of the basics of μSR will be given in the next section.

Chapter 2

Experimental Methods

We now proceed to describe the setup and procedures of this experiment. We also explain why we decided to use Muon Spin Relaxation for this experiment, and not some other technique. We further describe the process used to generate muons in sufficient quantities for this experiment and the procedure for implanting these muons, including a discussion on muonic decay.

2.1 Muon Spin Relaxation

2.1.1 Advantages of Muon Spin Relaxation

Muon Spin Relaxation (μSR) offers an unparalleled ability to probe the internal magnetic structure of condensed materials. Although similar enough in principle to other nuclear probing techniques, such as Nuclear magnetic resonance (the technology used in hospital MRI machines) or electron spin resonance, μSR offers the additional benefit of providing results in time-space, rather than frequency space [13].

Additional benefits resolve from the fact that the research muons used are spin-polarized at their source. As a result, μSR techniques can be used regardless of the magnetic nature of the material,

and experiments can be performed without an external magnetic field to "sort" the muons into the right state [5]. We can then test our substance in a variety of magnetic fields, without worrying that the applied field will inadvertently affect the muons' spin before their decay into positrons.

Finally, μSR provides an excellent holistic description of the sample being tested, not just in one specific location. As the muon's spin is particularly sensitive to even weak magnetic interactions, μSR is an excellent technique for measuring the magnetic behavior of substances exhibiting multiple internal magnetic behaviors at once. Since the muon's final implantation occurs at a random interstitial site inside the material's crystal lattice, the magnetic behavior of the full sample can be correctly described [5].

2.2 Muon Generation

2.2.1 The Consistent Muon Source

Although the aforementioned Cosmic Rays described by Theodore Wulf provide a natural source of muons[1], muons can also be artificially generated for research purposes in far greater quantities through the use of particle accelerators.

In our experimental set-up, a *cyclotron* was used to create a constant stream of high-energy protons (p). These high-energy protons were then collided into a 10 cm Beryllium target (Designated 1AT2 in figure 1) [15]. These collisions generated pions, a type of particle known as a *meson* composed of a quark and an anti-quark, under the following process [5]...

$$p + p \rightarrow p + n + \pi^+$$

$$p + n \rightarrow p + p + \pi^-$$

By artificially constraining our proton beam to a certain energy band such that the incoming protons

[1] the vertical intensity is about 1 muon per square centimeter per minute [14]

had just enough energy to reach the target nuclei, the resulting pions were relatively low energy (on the order of 4.1 MeV) and momentum (29.5 $\pm$ 3 MeV/c at the TRIUMF facility where we performed our experiments) [5] [15]. As a result, the generated pions could not escape from their generative substance. The surrounding atoms swiftly captured any unwanted negative pions, leaving only the desired positive muons behind, which decayed under the following process...

$$\pi^+ \rightarrow \mu^+ + \nu_\mu$$

This occurred before the positive pion could escape from the target. Since only the positive muons and neutrinos reached the surface of the target, the generated muons are known as *surface muons* [5].

All of the μSR data in this paper were obtained with the help of the TRIUMF laboratory in Vancouver, British Columbia on their M20D beamline [16], one of the few facilities worldwide with sufficient material requirements to construct a photon source with enough energy.

Figure 2.1 TRIMUF cyclotron

2.2.2 Spin Polarization

Beyond the high quantities of positive muons emitted relative to negative muons, a particular benefit of using surface muons is that the resultant muon beam is also highly spin-polarized. The decay process undergone by a positive pion creates both a positive muon and a muon neutrino. An important property of neutrinos is that their spin must always be aligned anti-parallel to their momentum, a behavior known as *negative helicity*. Furthermore, a decaying pion must create two particles, that, in the reference frame of the pion, have exactly equal and opposite momenta. Since the pion has zero spin, and the neutrino's spin is anti-parallel to its momentum, the muon *must* also have a spin anti-parallel to its momentum, thus preserving the conservation of momentum. As a result, the beam of surface muons created by ours set up, under ideal conditions, had near 100 percent spin polarization [3].

2.3 Muon Implantation Procedure

2.3.1 Muon Transport

The emitted beam of positive muons was then conveyed from the 1AT2 target down the M20D beamline to a LAMPF spectrometer (see Figure 2.1). Since the muon has both charge and spin, a muon beamline can be focused through the use of Quadripole magnets. Each Quaudripole magnet is used to focus the muon beamline in either the x or y axes. Several quadripole magnets are used in series [5], similar to the consecutive lenses in a high-quality camera like the ones you see clustered behind the end zones of professional football games.

As these magnetic "lenses" focused any charged and spinning particle into the muon beamline, dipole magnets were also used as a kind of "filter." These magnets end up curving the beam, with the radius of curvature depending on the mass of the particle being affected. This can then be used to filter out unwanted particles (like free protons), which will deflect in the dipole field at differing

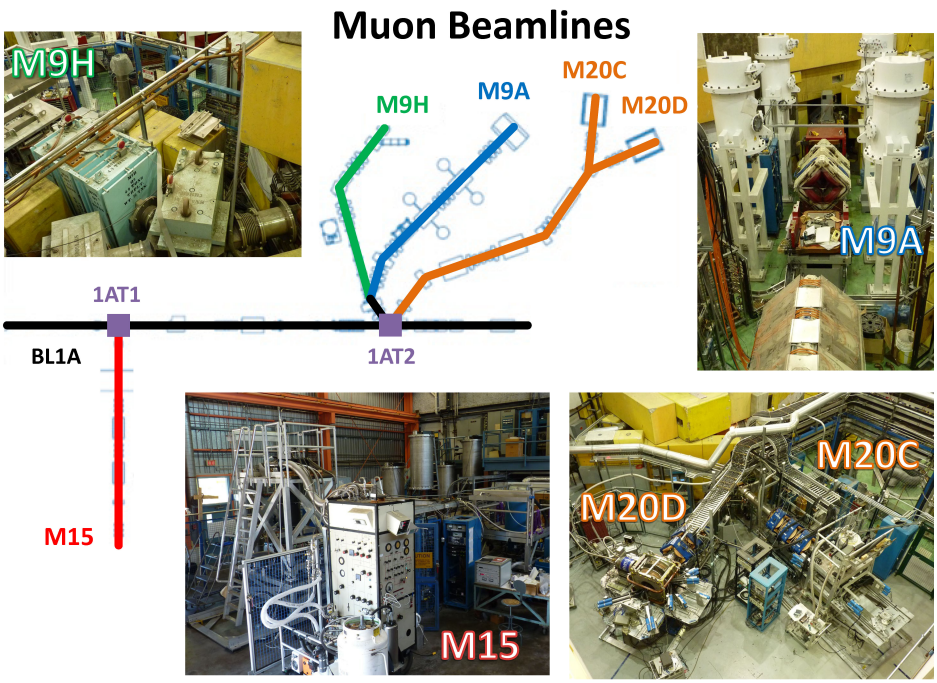

Figure 2.2 Beamlines at TRIUMF [15]

angles than the positive muons. We selected the correct angle for our curve such that only positive muons remained in our beamline[2]. Furthermore, Momentum Slits were used to filter out particles without the correct momentum described previously in this chapter. A separator, a device with two electrically charged plates and a dipole magnet that creates tuned electric and magnetic fields, was used to separate out positron contamination. [5].

2.3.2 Post Implantation Behavior

The muons were then implanted into our sample of $CoTa_2O_6$, which was kept at the desired testing temperature in a liquid-helium-cooled cryostat with thin windows [5]. Upon implantation into the material, muons shed most of their energy by ionizing nearby atoms and scattering nearby

[2]In addition, dipole magnets were used when the beamline just needed to be bent to fit the geometry of the experiment. One can see the bends along beamline M20D in Figure 2.1

electrons on their path through the sample[3], dropping down to an individual energy of only a few Kilo-electron-volts [3] and coming to rest at an *interstial* site (open space in the crystal lattice) [13].

They then began a sequence of electron capture and release reactions, which further reduced their energy to only a few hundred electron volts. This entire chain of events took place in a matter of about 100 picoseconds to 1 nanosecond. As this process is so rapid, the implanted muons thermalized with the $CoTa_2O_6$ before they decayed themselves [3].

The muon has a useful *lifetime* (the average time until particle decay) of 2.18 μs. This means that soon after implantation and thermalization, a positive muon decays into a positron (a positive electron), an electron neutrino, and a muon anti-neutrino under the following process...

$$\mu^+ \rightarrow e^+ + \nu_e + \bar{\nu}_\mu \tag{2.1}$$

Importantly, this decay involves the weak interaction and has the important property that *parity* is not conserved (the weak interaction also causes the negative helicity of the neutrino discussed previously). In layman's terms, this means that the emitted positron (e^+) is most likely to be emitted in the same direction as the muon's spin vector. Thus by detecting these emitted positions, we were able to determine the probable direction of our implanted muon's spin. By implanting enough muons to create many positrons, we were able to alleviate the probabilistic nature of this detection.

2.4 Detection Array

2.4.1 Positron Detection Procedure

Positron emissions were detected by a LAMPF[4] spectrometer, which is permanently installed on the M20D beamline [15]. The internal magnetic coils of this spectrometer were used to either apply

[3] As discussed in section 1.2

[4] Los Alamos Meson Physics Facility

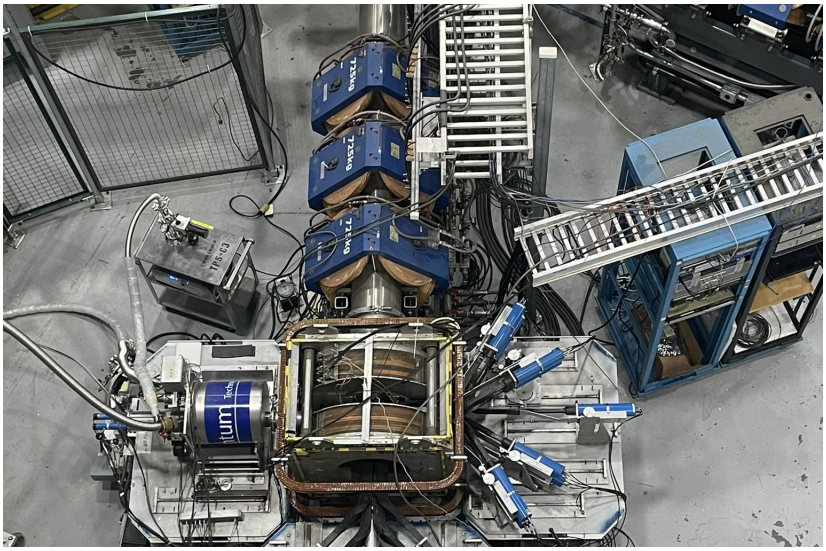

Figure 2.3 Omni-LAMPF Spectrometer (taken by the author)

a longitudinal or transverse magnetic field relative to the muon's momentum or else to zero out the external magnetic field [17]. Positron detectors were arranged symmetrically, both ahead and behind the sample relative to the beamline. These two detectors were called the forward and back detectors respectively.

A muon detector was also used to determine whether a muon has entered the sample [5]. If a second muon entered the sample before the first muon had decayed into a positron and been detected, the data point was discarded, since it is impossible to tell whether the first or second muon had decayed, and thus measure the correct decay time [3]. The positron detectors were capable of generating a time-stamped electrical signal with picosecond timing for precise measurement of the muon decay time [5].

2.4.2 Mathematical Asymmetry

The primary experimental value we were measuring was the asymmetry as a function of decay time, which is time needed for each muon to decay and be detected after implantation. This asymmetry

was calculated as follows...

$$A(t) = a_0 G_z(t) = \frac{N_F(t) - \alpha N_B(t)}{N_F(t) - \alpha N_B(t)} \tag{2.2}$$

where

- $N(T)$ is the number of positions detected in time bin $t + \Delta t$ relative to implantation (for each detector respectively).
- α is a calibration constant determined through testing of examination of a known material
- a_0 is the empirical maximum for the spectrometer [5].

This equation is known as the *relaxation function*. For these experiments, the empirical maximum was set to be $a_0 = 0.25$ [18]. The calibration constant α will be discussed in the following section.

When a muon is implanted into the crystal, its spin vector is subject to a variety of random quantum fluctuations. The longer it takes for a muon to decay, the more likely it is that its spin will change from its initial polarization. As a result, the asymmetry function will decay exponentially, as particularly long-lived muons are almost as likely to spin forward as they are to spin backward. It's this "relaxation" behavior that gives μSR its name.

2.4.3 Calibration

By fitting a curve to the μSR output data of a control run, whose μSR behavior is known, the calibration constant α can be determined. It should be noted that this value does change slightly depending on how large your time binning (Δt) is. The calibration constant in these experiments was determined using $CoTa_2O_6$ at 60K in a weak transverse field of 30 Gauss [18].

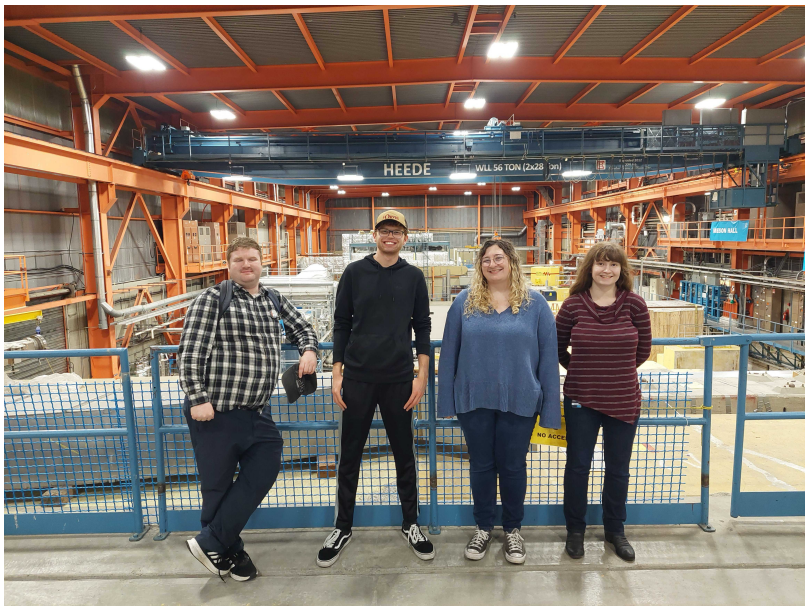

Figure 2.4 TRIMUF Research Team

Chapter 3

Experimental Results

In this section, we describe the three different orientations of an external magnetic field we tested our sample of $CoTa_2O_6$in: No external magnetic field, a longitudinal field of 4000G, and a transverse field of 30G. With our positron detectors placed in front of and behind our samples (rather than on either side), we cannot apply a stronger transverse field without affecting the incoming muon spin polarization, if not bending the beamline completely out of the LAMPF spectrometer.

By comparison with the control data set described in section 2.4.3, we were able to determine the following calibration constants α, which are set out in Table 3.1. The calibration constants were set for each time bin Δt individually at the beginning of fitting.

Δt	α
150 ns	1.09236
100ns	1.09216
5ns	1.09247
1ns	1.09236

Table 3.1 Calibration Values

Our sample of $CoTa_2O_6$ transitions from exhibiting paramagnetic behavior to exhibiting antiferromagnetic behavior as it cools. This transition occurs and the sample approaches the Neel temperature (T_N). Our experiments here determine that the Neel temperature is around $T_N = 7.926$K, as we will discuss later[1].

3.1 Zero-Field Results for $CoTa_2O_6$

3.1.1 Zero Field Behavior

For our first set of runs, the internal magnetic coils of the LAMPF spectrometer were used to zero out any external magnetic field. As a result, the internal magnetic moments in the sample are solely the result of the internal magnetic domains, and not from any outside interactions. The minimum tested temperature was 2K, while the maximum tested temperature was 60K.

[1] See section 3.2.2

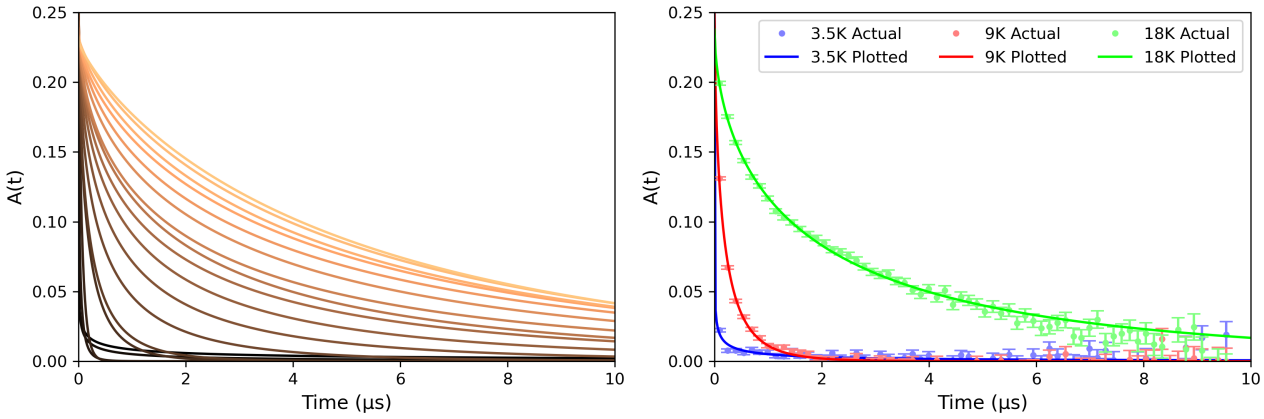

(a) **(b)**

Figure 3.1 Zero-Field Results: **(a)** is all 18 curves generated plotted on the same plot, with warmer colors representing (relatively) warmer temperatures. **(b)** shows three selected curves near the Neel temperature plotted alongside the respective raw data that created each curve. Our time binning Δt=150 ns for both plots.

After receiving the run data from TRIUMF [16], we set a curve to it using the following stretched exponential fitting function,

$$A(t) = ae^{-(\lambda t)^{\beta}} \tag{3.1}$$

With fitting parameters a, λ, and β. Because of our set-up empirical maximum, we restricted a to fall between 0 and 0.25, while λ and β were restricted to positive real numbers.

We varied the temperature for each run. The resulting curves (With the found parameters in the correct place, and a time binning Δt of 150ns) are plotted in Figure 3.1.a, with the highest temperatures having the shallowest curves. As we can see, the relaxation rate of the asymmetry function increases as the temperature decreases, as the internal magnetic order of the sample asserts its influence in shorter and shorter intervals. Figure 3.1.b shows three selected curves plotted alongside the raw asymmetry data used to fit the curves.

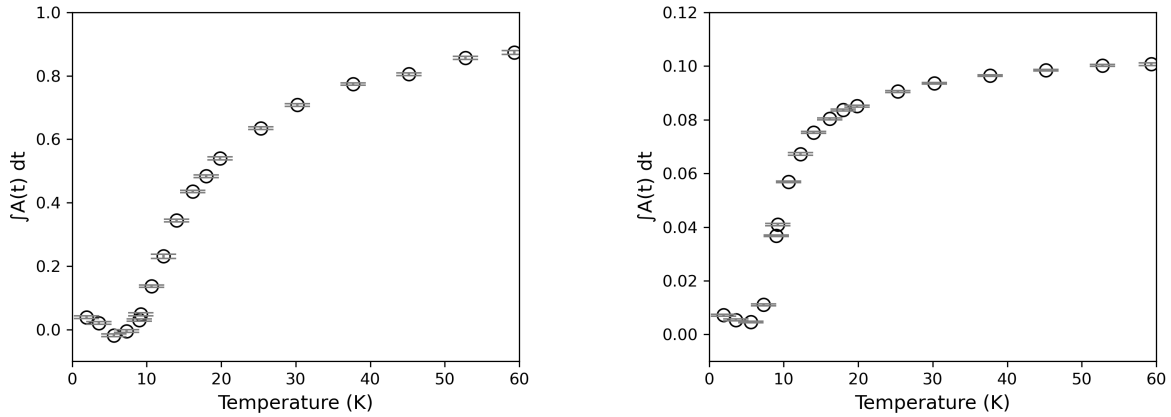

(a) **(b)**

Figure 3.2 Integrated Asymmetry: **(a)** is the raw data integrated with Δt =150ns. **(b)** is the raw data integrated with Δt =5ns. As our sample of $CoTa_2$

3.1.2 The Turning Point in a Zero Field

The decrease of the fitted curve up just above the Neel Temperature is fairly consistent[2], with β declining from 0.75 to 0.56 and λ increasing from 0.204 to 2.55. Beyond this point, however, the fits become far less reliable, as the uncertainties of λ (our relaxation rate) become multiple magnitudes greater than the value itself (at 3.5K, $\varepsilon(\lambda) = 7669$, see Figure 3.3). In contrast, the values of β vary in an unstable fashion. At these low temperatures, the asymmetry asymptotically drops to zero so quickly that only the first few points are available to fit the relaxation. With so little data available, uncertainties naturally grow.

Decreasing the time binning (Δt) selected can alleviate this problem. By decreasing Δt to 1ns (the minimum used by our analysis software[3]), we can lower the value of λ to 41.6, and increase the value of β to 1.2. These parameters are at least more rational but still not perfect.

That said, we don't want to ignore the forest for the trees. A quixotic focus on fitting parameters is not our best bet in this situation, as we can see qualitatively in Figure 3.1. Despite the rapid

[2]See Appendix A for fit data tables

[3]See Appendix B for more details

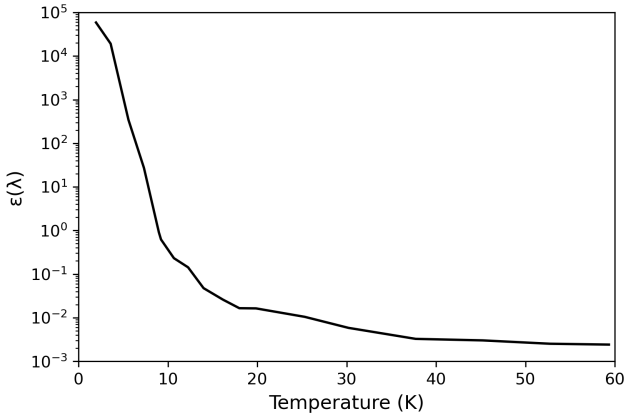

Figure 3.3 The growth in the error of the lambda parameter as a function of temperature, plotted with respect to the Temperature of our sample.

increase in λ and the rapid decrease in β, we can see that the overall relaxation curve changes a little past the Neel temperature (enough so that the 100ns fits used in Figure 3.1 overlap with each other). Our fitting parameters don't show this, but that's to be expected, given the nature of our fitting function: past a certain point, increases in λ don't affect the curve as much. A better way of determining our magnetic evolution at the Neel temperature is to numerically integrate the raw μSR data. In Figure 3.2, we can see this integration performed for both 150ns and 5ns. As we can see in the 5ns integration, the change in asymmetry due to temperature has almost completely flatlined (and has slightly increased at the lowest temperature in the 150ns range). We'll discuss what this all might mean in Chapter 4.

3.2 Strong Longitudinal Field

3.2.1 Longitudinal Field Behavior

For our second testing run, we used the internal magnetic coils of the LAMPF spectrometer to impose a strong external field of 4000G or 0.4T [16]. This is a fairly strong field and will have a substantial effect on the results. The field was aligned such that it was parallel to the incoming muon's momentum (and hence, anti-parallel to the muon's spin). Thus, we call this field arrangement a *longitudinal field*. 15 temperatures were tested, varying from 70K to 2K, encompassing both paramagnetic and antiferromagnetic behaviors.

We then reused the following fitting function from our Zero-Field Results,

$$A(t) = ae^{-(\lambda t)^{\beta}} \tag{3.2}$$

and best fit a curve to the raw output data. Once again, we restricted α to between 0 and 0.25, while also restricting β and λ to be positive real numbers. The resulting curves (for time binning Δt =150ns) are plotted in Figure 3.4.a, with three selected curves plotted alongside their respective

fitting data in Figure 3.4.b.

3.2.2 The Turning Point in a Longitudinal Field

For temperatures above the Neel temperature (T_N) the relaxation function followed the same general pattern as the Zero Field results: an exponential decay over time. As the temperature decreased the rate of exponential decay respectively increased. Below the Neel Temperature, however, an unusual behavior manifests itself. Although the overall function still decays exponentially, the asymptote is no longer at $A(t) = 0$. Instead, as the temperature decreases, *both* the rate of decay (λ) and the asymptote value increase, with the asymptote reaching a maximum of about $A(t) = 0.05$ at T =2K.

We can see this behavior reflected in the integrated asymmetry, shown in Figure 3.5. As we can see, $\int A(t)\,dt$ reaches its minimum at the Neel Temperature, before increasing sharply as the

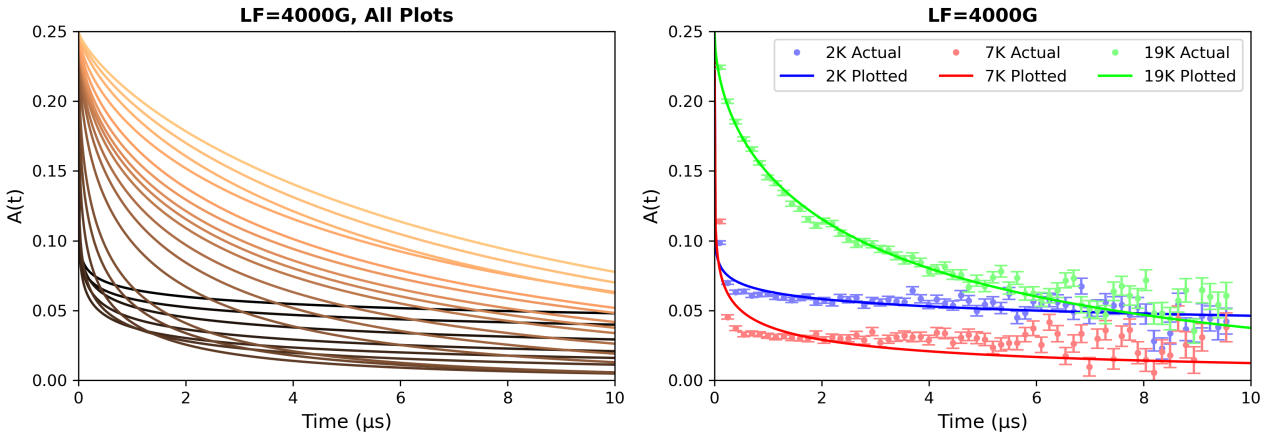

(a) **(b)**

Figure 3.4 Longitudinal Field Results: **(a)** is all 21 curves, from 70K to 2K, generated and plotted on the same axes, with warmer colors representing (relatively) warmer temperatures. These measurements were taken in a transverse magnetic field of 4000G. **(b)** Shows three selected curves near the Neel temperature plotted alongside the respective raw data that created each curve. Our time binning Δt =150ns for both plots.

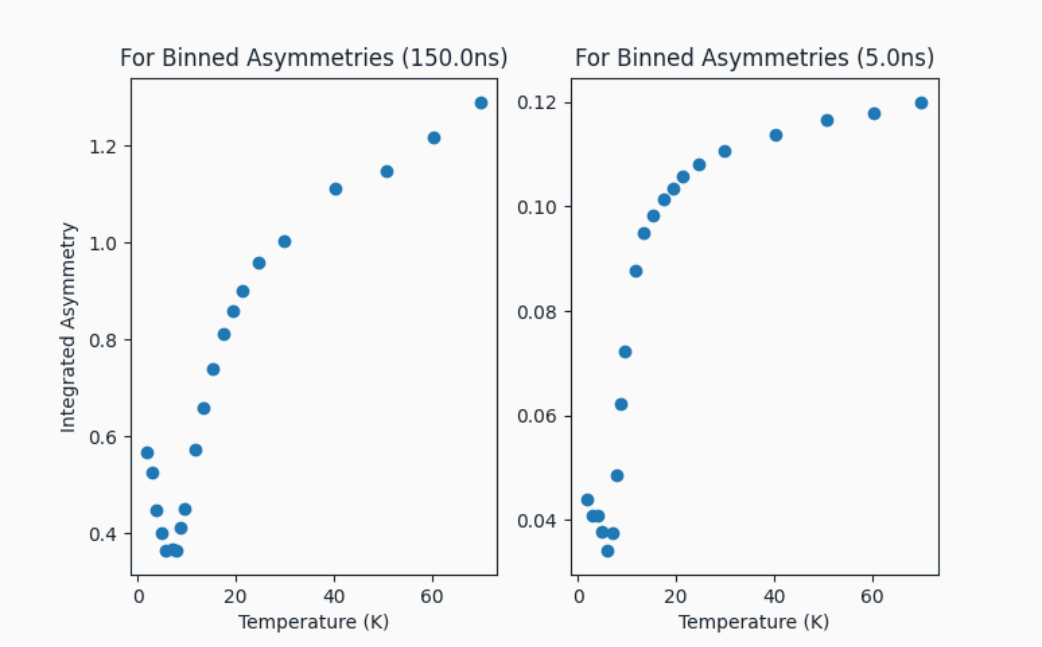

Figure 3.5 Integrated asymmetry for both Δt=150ns and Δt =5 ns, plotted with respect to temperature.

temperature decreases (as an exponential function with a higher asymptote will have a greater area under the curve)[4]. This behavior is visible in both the Δt =150ns and the Δt =5ns domains, so it's not an effect of the time binning choice, and instead represents the external field overwhelming the local magnetic moments of the individual microscopic domains[5].

3.3 Weak Transverse Field

3.3.1 Weak Transverse Field Behavior

For our final testing set, we used the magnetic coils of the LAMPF spectrometer to create a weak magnetic field of 30G [16]. This field was aligned orthogonal to the incoming muons' momentum

[4] In fact, it's this sharp point that helped us to determine the Neel temperature for this experiment in the first place, and propose our slightly higher value

[5] See Chapter 4

vector, and as a result, is called a *transverese field*. As discussed in Chapter 1, this field orientation will apply a torque to the incoming muons, causing the spin vector to precess gyroscopically, like a spinning top. The temperature tested varied from 2k to 60K[6].

The behavior of the relaxation function in this field orientation requires a piecewise-defined fitting function, as the behavior of A(t) varies dramatically from paramatnetic to antiferromagnetic local order.

$$A(t) = aH(T_N)\cos\left(2\pi vt + \frac{\pi\phi}{180}\right)e^{-\beta t} + de^{-\lambda t} \tag{3.3}$$

Where $H(T_N)$ is the Heaviside step function, defined as 0 if $T < T_N$ and 1 if $T \geq T_N$. a and d were both restricted to be between 0 and 0.25[7], while v, ϕ, β, and λ were restricted to be positive real numbers. The fit curves (for time binning Δt =150ns) are plotted in Figure 3.6.a. Three selected curves, displaying the relaxation function's behavior around the Neel temperature, are plotted in Figure 3.6.b.

3.3.2 The Turning Point in a Weak Transverse Field

When constrained in a transverse magnetic field $CoTa_2O_6$ displays two distinct behaviors, exponential decay, and oscillation, which correlate to antiferromagnetic and paramagnetic local order respectively. This is not a hard transition, however, as antiferromagnetic and paramagnetic behavior is determined by how the domains are aligning at the atomic level. The Neel temperature is simply the point at which all of the individual magnetic domains are aligned counter to one another.

In the temperatures above the Neel temperature, our sample is displaying both behaviors in some quantity, a factor represented by our twin asymmetry maxima a and d (as these aren't real maxima anymore, I tend to call them behavior coefficients.). As a result, our sample of $CoTa_2O_6$.

[6]It was this 60K test that was used to calibrate our α values

[7]In reality, $0.25 \geq \sqrt{a^2+d^2}$ is the true empirical maximum, but we could find no way to directly impose this condition in our fitting software

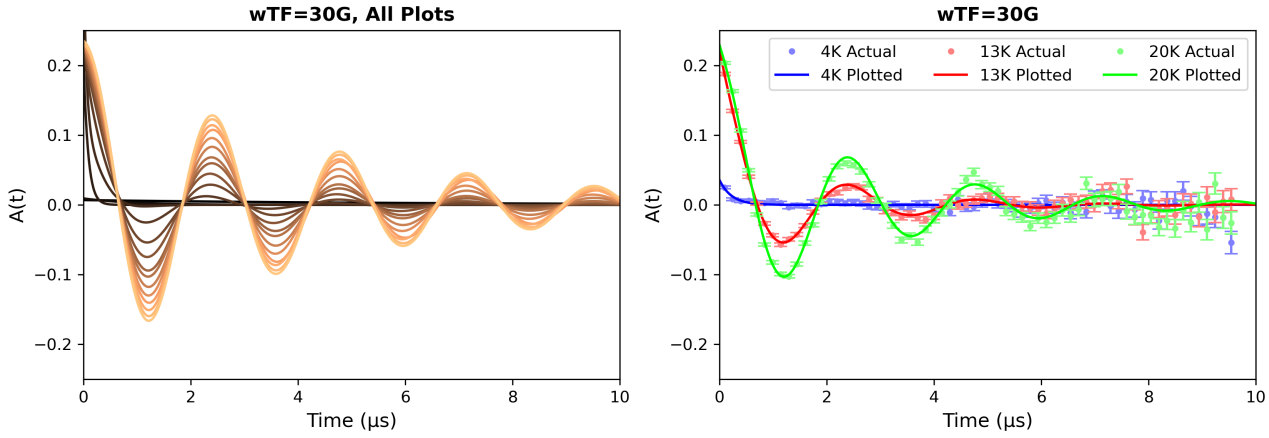

(a) **(b)**

Figure 3.6 Weak Transverse Field Results: **(a)** is all 15 curves, from 60K to 2K, fit and plotted on the same axes, with warmer colors representing (relatively) warmer temperatures. **(b)** shows three selected curves around the Neel temperature plotted alongside the respective raw data that created each curve, and where we can see the evolution from exponential decay to oscillation. Our time binning Δt =150ns for both plots.

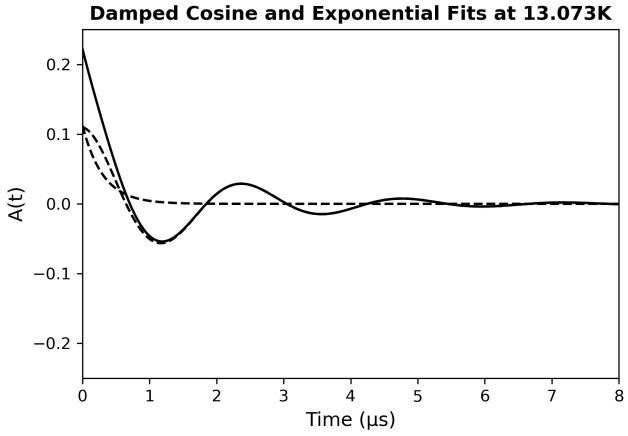

Figure 3.7 The breakdown of our behavior at 13K. The dashed lines are the individual paramagnetic and antiferromagnetic behaviors, while the solid line is the overall relaxation function.

The summation of these two behaviors can be seen in Figure 3.7, which plots both behaviors at 13.7K. This type of analysis is one of the advantages of μSR, as the relaxation function produced

is a summary of the behavior of the entire sample, and not just one part, allowing a more holistic description of a sample exhibiting multiple magnetic behaviors.

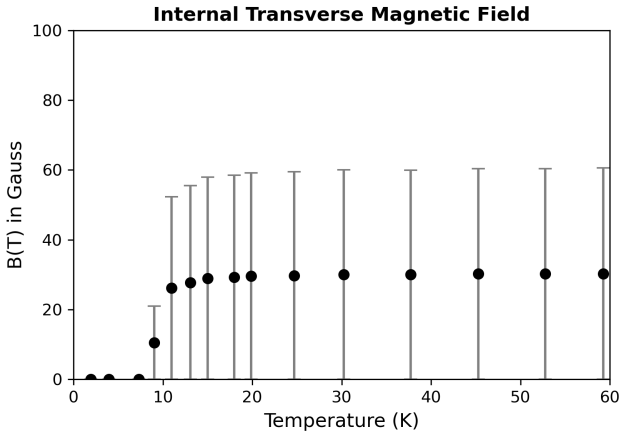

Figure 3.8 The magnitude of the internal transverse magnetic field. The transition begins near 15K and ends at the Neel temperature T_N =7.926.

3.3.3 The Internal Magnetic Field

This changing behavior is linked to the evolving magnitude of the overall internal magnetic field. In the above fitting equation, the parameter *v* represents the *Larmor Frequency* of muons precessing in a magnetic field. Since the Larmor frequency is directly proportional to the strength of the transverse magnetic field (equation 1.5) at our muon sites, we can use this fitting parameter to calculate the magnitude of the internal field, which is plotted in Figure 3.8.

While the calculated nature of these values leads to a high degree of uncertainty (all the uncertainty values get multiplied), we can ascertain the general shape of the curve. This curve confirms our previous observation that the magnetic transition at the Neel Temperature is not hard, as the magnitude of the magnetic field begins to weaken at 15K.

Chapter 4

Conclusions

We now discuss a few conclusions we have derived from the data presented above. We start with a discussion on the location of the Neel Temperature, before moving on to some interesting observations about the behavior of $CoTa_2O_6$ while exhibiting antiferromagnetic behavior

4.1 Examining The Turning Point

4.1.1 The Experimental Neel Temperature

The numerical integrated asymmetry data presented in Figure 3.5 has a global minimum in the low single-digits kelvin. When the time binning is 150ns, the integration has a broad minimum between 5.867K and 7.926K[1]. In the 5ns range, this point is sharpened, such that the minimum falls at 5.867K, with an integrated uncertainty of $\int A\,dt = 0.03415 \pm 0.0036$[2]. Since the accuracy of numerical integration methods increases the smaller Δt gets (we are essentially finding the area of thinner and thinner rectangles), we take the 5ns integration to be the more reliable of the two.

That said, it should not be forgotten that we are dealing with a limited data set and that the

[1] See Appendix A, Table 3

[2] See Appendix A, Table 4

actual low point of $\int A\,dt$ could vary from 4.987K to 6.993K (the two points on either side of the minimum. The X-ray diffraction analysis performed by R.Baral et al proposed that $CoTa_2O_6$ had a Neel Temperature around $T_N = 6.6K$, which was derived from analysis of the substance crystal structure, and not an analysis of its magnetic field. Our experimentally determined Neel Temperature aligns with this proposition, with the expected Neel Temperature falling in the upper end of our range.

4.1.2 Local Magnetic Field Strength as a Function of Temperature

Another valid point is the soft transition between paramagnetic and anti-ferromagnetic order in the substance. As we can see in Figure 3.8 in the last section, the internal magnetic field begins to weaken about 15K, finally reaching zero around the Neel Temperature. This behavior aligns with the fact that the Neel Temperature is when the sample of $CoTa_2O_6$ is demonstrating primarily paramagnetic behavior to primarily antiferromagnetic behavior, with most of its domains are counter-aligned to one another(see Fig 4.1), a phenomenon sometimes called saturation.

4.2 Anti-Ferromagnetic Behavior

4.2.1 Stable Asymmetry Below the Neel Temperture

The behavior below the Neel Temperature for both our Zero Field and Weak Transverse Field samples is relatively straightforward. As the temperature decreases, both samples exhibit zero asymmetry in shorter and shorter periods, and the exponential decay of the response function (represented by the λ fitting parameter) increases dramatically. This is caused by the evolution of the internal magnetic domains of the sample. As the temperature approaches absolute zero, the various domains of the material grow in size [2]. This can be described as a reduction of entropy at the atomic level, as atoms on the borders between domains increasingly choose certain domains

over others (imagine dividing a large number of people into 4 groups instead of 400. You are going to get a far greater amount of people per group) [1]. Since larger domains have larger magnetic fields (more electrons per domain), the strength of the internal magnetic field at any given point inside the samples is inversely proportional to the sample's temperature.

This increase in the microscopic field strength does not have a holistic effect on the macroscopic field. At low temperatures our sample of $CoTa_2O_6$ is behaving in a predominantly antiferromagnetic behavior. Thus, even though the individual domains of the sample are larger, they are still predominantly aligned counter to one another. Since the 1-dimensional lattice structure of $CoTa_2O_6$[3] forces each magnetic dipole into only a single degree of freedom, each domain will be aligned anti-parallel to its neighbors. The overall result of this is that 50% of the sample's domains will have a forward alignment and 50% will have a backward alignment. As a result, any implanted muon has an equal chance of emitting a positron either forward or backward once aligned with the local dipole moment. The stronger the magnetic field at each implantation site, the shorter the time needed to align the muon's spin with this local dipole moment. The visible result of this effect is the rapid increase in exponential decay in the response function as the sample temperature approaches absolute zero [18].

4.2.2 Oscillating Behavior In a Weak Transverse Field

. As shown in Fig 3.6.a, the material placed in a weak transverse field displays an oscillating behavior above the Neel Temperature. This oscillating behavior is due to the Larmor Precession of the muon's spin[4], as described previously. Below the Neel Temperature, however, this oscillating behavior dies out to the point that including the trigonometric function in the fitting equation (equation 3.3) results in a less accurate fit[5].

[3] See sec 1.3

[4] See sec 1.2

[5] This is why we included the *Heaviside Function* in equation 3.3, zeroing out the dampened cosine function below the Neel Temperature)

This happens because, at low temperatures, the individual magnetic field strength of each domain is orders of magnitude greater than the applied magnetic field (on the order of 1 Tesla) [18]. As a result, the applied magnetic field can be effectively ignored, the material behaves like there is no applied magnetic field. As discussed in section 4.1, this is not a hard transition, and the gradual increase in antiferromagnetic behavior as the material approaches the magnetic transition accounts for the dampened nature of the oscillating behavior at temperatures above but near the Neel Temperature.

4.2.3 Increasing Asymmetry At Low Temperatures in A Strong Longitudinal Field

Past the Neel Temperature, the sample of $CoTa_2O_6$ placed in a strong longitudinal magnetic field exhibits a somewhat counter-intuitive behavior: The asymptote of the exponential decay function is no longer zero. As shown in Table 4.1, this asymptote ranges to about 0.063. As our empirical maximum asymmetry was set[6] to be 0.25, this is a fairly significant change.

A potential explanation for this behavior is an interaction between the growing magnetic domains and the external magnetic field. As the individual domains grow in population (the number of atoms in each domain), The overall number of domains must decrease: returning to our example from section 4.2.1, if we are dividing a group of 400 people such that we have 100 people per division, we will only have four overall divisions. If we change to 10 people per group, we will have 40 divisions. This reduction in the number of domains allows individual anomalies in the domain structure to have a greater effect on the response function.

We turn to statistical mechanics for a further explanation of the phenomenon. Since the lower end of our temperature scale is where antiferromagnetic behavior is strongest, the overall preference of our domains is to remain anti-parallel to their neighbors (restricted of course, by the crystalline

[6] See section 2.4.2

T (K)	ΔT	d parameter	Δd
1.940	0.007	0.06316	0.00080
2.911	0.032	0.05752	0.00079
3.948	0.007	0.05582	0.00076
4.987	0.010	0.04551	0.00093
5.867	0.007	0.03442	0.00077
6.993	0.011	0.03326	0.00082
7.926	0.006	0.03269	0.00126
8.803	0.010	0.03885	0.00381
9.659	0.006	0.03354	0.00935

Table 4.1 Increasing Asymptotic Behavior in a Strong Longitudinal Field

structure described above[7]). That said, in a strong enough external magnetic field, a few domains may express paramagnetic behavior rather than anti-ferromagnetic behavior even below the Neel Temperature: Remember that the Neel Temperature is not a hard transition. When coupled with a small number of domains, the effect of only a few domains swapping to align with the external magnetic field (paramagnetic behavior) is much more pronounced. This is to be expected, as with fewer choices, a greater deviation from the most probable state is to be expected[8]. As a result, our

[7] See sec 1.3

[8] A simple thought experiment can help us explain this result. When a coin is flipped it has a 0.5 probability of being either heads or tails. That said, it is not unheard of that someone might flip the same coin 3 times and each time get heads (this happens statistically 0.8% of the time). At the same time, one would not expect to flip the same coin 50,000 times and get the heads each time. The small sample size increases the probability of strong deviations from the most probable state, as the number of possible results from flipping a coin 3 times is much lower than the number of results from flipping a coin 50,000 times. Now imagine that our coin is weighted slightly towards one side, We would extend this to have a dramatic effect on a small number of flips, while a reduced effect on a large number of flips

sample, although still acting in an increasingly antiferromagnetic state, actually becomes less able to zero out the strong external magnetic field [18].

4.3 Further Study

It should be noted here that my research into the internal magnetic properties of $CoTa_2O_6$ is only one part of a bi-fold project, with a further analysis provided using Powder Neutron Diffraction (PND) techniques. While the results and analysis of those tests are not presented in this thesis, they will be present when this research is eventually published. As a result, a PND analysis of low temperature $CoTa_2O_6$ is the obvious next step in our research. We expect that research to be finished sometime this fall, with the eventual publication in an appropriate journal occurring sometime next year.

Appendix A

Fitting Data Tables

The raw data behind the fits given in Chapter 3 is presented here.

T	ΔT	a	Δa	β	$\Delta\beta$	λ	$\Delta\lambda$
1.958	0	0.25	0.71042	0.146	0.13693	4313.47797	58802.03979
3.596	0.03	0.25	0.68918	0.18065	0.15281	1863.12249	19194.00836
5.587	0.015	0.25	1.26658	0.53145	0.88148	51.20476	345.48557
7.325	0.014	0.25	0.44815	0.89647	0.77284	15.32291	27.05403
8.991	0.014	0.25	0.0229	0.64212	0.04767	5.83538	0.90771
9.229	0.012	0.25	0.01729	0.61233	0.03552	4.99631	0.62172
10.672	0.017	0.25	0.01101	0.55589	0.02416	2.54851	0.23141
12.259	0.015	0.25	0.0108	0.53644	0.02625	1.52014	0.14267
13.992	0.015	0.25	0.00534	0.53025	0.01451	1.01028	0.04748
16.159	0.012	0.25	0.00395	0.52373	0.01167	0.74509	0.0259
17.994	0.014	0.23772	0.00357	0.57473	0.01418	0.5455	0.01647
19.856	0.011	0.24341	0.00387	0.54651	0.01444	0.49714	0.01631
25.308	0.031	0.2387	0.00378	0.58985	0.01833	0.35577	0.01044
30.204	0.016	0.23855	0.00275	0.61362	0.0155	0.29047	0.00583
37.719	0.036	0.23304	0.00196	0.67822	0.01443	0.2396	0.00326
45.2	0.11	0.23345	0.00196	0.71867	0.0163	0.22476	0.00301
52.758	0.023	0.2329	0.00177	0.76316	0.0171	0.20417	0.00252
59.34	0.24	0.22966	0.00169	0.81724	0.01921	0.19259	0.00241

Table A.1 Zero Field Fitting Parameters, $\Delta t = 150$ns

T	ΔT	a	Δa	β	$\Delta\beta$	d	Δd	λ	$\Delta\lambda$
1.94	0.007	0.25	0.08122	0.75377	0.16952	0.06316	0.0008	33.86553	14.58023
2.911	0.032	0.25	0.06953	0.8056	0.16455	0.05752	0.00079	30.74938	10.8678
3.948	0.007	0.25	0.06545	0.80441	0.15548	0.05582	0.00076	30.32858	10.12334
4.987	0.01	0.25	0.0579	0.78314	0.14273	0.04551	0.00093	25.3677	7.84368
5.867	0.007	0.25	0.03522	0.80799	0.09743	0.03442	0.00077	21.03162	3.93646
6.993	0.011	0.25	0.01998	0.94174	0.08048	0.03326	0.00082	14.31681	1.40051
7.926	0.006	0.25	0.01357	0.81191	0.0519	0.03269	0.00126	8.9409	0.62682
8.803	0.01	0.23445	0.01683	0.72504	0.06736	0.03885	0.00381	5.68656	0.41409
9.659	0.006	0.2295	0.01994	0.70129	0.07792	0.03354	0.00935	3.35303	0.24167

Table A.2 Strong Longitudinal Field Fitting Parameters, $\Delta t = 150$ns

T	ΔT	a	Δa	λ	$\Delta\lambda$	d	Δd	ϕ	$\Delta\phi$
1.947	0.012	0.04635	50353.96502	0.15725	0.14233	0.00683	0.00259	-40.02424	74122117
3.945	0.013	0.24999	10625.59733	1.11829	0.94622	0.00918	0.01029	70.93567	840227.77
7.321	0.014	0.14694	41925.02378	11.68878	1.69264	0.20808	0.02935	90.82765	236155.04
9.041	0.01	0.13313	0.04419	18.12491	36.70755	0.25	0.46616	-36.91827	82.0903
10.969	0.009	0.0608	0.00689	3.85464	0.49419	0.16299	0.01039	-10.77483	10.4455
13.073	0.009	0.11074	0.00633	3.26588	0.57931	0.11233	0.01105	-7.4986	5.55721
15.017	0.009	0.13235	0.00432	3.44149	0.54103	0.09311	0.00818	-9.11003	2.96729
17.995	0.009	0.1535	0.00491	3.91117	0.88237	0.07776	0.00939	-10.3231	2.57441
19.856	0.009	0.16012	0.00502	3.72247	0.96372	0.07124	0.01023	-9.37095	2.60608
24.67	0.06	0.17054	0.00399	3.84643	0.89113	0.06636	0.00865	-10.12676	1.84704
30.216	0.005	0.18117	0.00313	3.26266	0.75767	0.04991	0.00704	-9.73953	1.40779
37.739	0.001	0.18785	0.00292	3.22196	0.71139	0.04987	0.00673	-8.87841	1.24083
45.31	0.025	0.2023	0.00272	4.20144	1.39627	0.03392	0.00642	-10.46257	0.97445
52.753	0.009	0.21162	0.00331	2.77198	1.54818	0.01968	0.00723	-9.67442	1.1497
59.269	0.002	0.21761	0.00323	5.00227	3.49625	0.02036	0.00812	-9.25542	0.9262

Table A.3 Caption

Bibliography

[1] D. J. Griffiths, *Introduction to electrodynamics*, fourth edition. ed. (Cambridge University Press, Cambridge, United Kingdom; New York, NY, 2017).

[2] Anonymous, in *A dictionary of physics.*, 4th ed. ed., A. Isaacs, ed., (Oxford University Press, Oxford; New York, 2000).

[3] S. J. Blundell, "Spin-polarized muons in condensed matter physics," Contemporary Physics **40,** 175–192 (1999).

[4] D. J. Griffiths, in *Introduction to quantum mechanics*, second edition ed., D. F. Schroeter, ed., (Cambridge University Press, Cambridge, United Kingdom, 2018).

[5] A. D. Hillier, S. J. Blundell, I. McKenzie, I. Umegaki, L. Shu, J. A. Wright, T. Prokscha, F. Bert, K. Shimomura, and A. Berlie, "Muon spin spectroscopy," Nature Reviews Methods Primers **2,** 4 (2022).

[6] MissMJ, "Standard Model of Elementary Particles,", 2013, cc by 3.0, via Wikimedia Commons.

[7] T. Wulf, "Uber die in der Atomsphare vorhandene Strahlung von hoher Durchdringungsfahigkeit," Physikalische Zeitschrift (in German) **10,** 152–157 (1909).

[8] T. Wulf, "Beobachtungen über die Strahlung hoher Durchdringungsfähigkeit auf dem Eiffelturm," Physikalische Zeitschrift (in German) **11,** 811–813 (1910).

[9] C. D. Anderson and S. H. Neddermeyer, "Cloud chamber observations of cosmic rays at 4300 meters elevation and near sea-level," Physical Review **50,** 263 (1936).

[10] R. Baral, H. S. Fierro, L. M. Martinez, S. R. Singamaneni, and H. S. Nair, "Low dimensional magnetism in the trirutile tantalates $Co_{1-x}Mg_xTa_2O_6$ with weak-ferromagnetic features," Journal of Applied Physics 125 (2019).

[11] R. K. Kremer and J. E. Greedan, "Magnetic ordering in CoTa2O6 and NiTa2O6," Journal of Solid State Chemistry **73,** 579–582 (1988).

[12] J. N. Reimers, J. E. Greedan, C. V. Stager, and R. Kremer, "Crystal structure and magnetism in CoSb2O6 and CoTa2O6," Journal of Solid State Chemistry **83,** 20–30 (1989).

[13] Y. J. Uemura, in *μSR relaxation functions in magnetic materials*, *Muon Science* (Routledge, 2017), pp. 85–114.

[14] P. D. Group, "Review of Particle Physics," The European Physical Journal C **3,** 1–794 (1998).

[15] I. McKenzie, "MuSR Beamlines at TRIUMF,", 2022.

[16] D. A. Jess H. Brewer, "Muon data access,", 2024.

[17] I. McKenzie, "Omni-Lampf,", 2021.

[18] F. Benjamin, "Research Meeting Notes,", 2024.

Index